

# Effective electrical manipulation of topological antiferromagnet by orbital

## Hall effect

Zhenyi Zheng<sup>1,6</sup>, Tao Zeng<sup>1,6</sup>, Tiejing Zhao<sup>1,6</sup>, Shu Shi<sup>1</sup>, Lizhu Ren<sup>2</sup>, Tongtong Zhang<sup>3</sup>, Lanxin Jia<sup>1</sup>, Youdi Gu<sup>1</sup>, Rui Xiao<sup>1</sup>, Hengan Zhou<sup>1</sup>, Qihan Zhang<sup>1</sup>, Jiaqi Lu<sup>1</sup>, Guilei Wang<sup>4</sup>, Chao Zhao<sup>4</sup>, Huihui Li<sup>4\*</sup>, Beng Kang Tay<sup>3\*</sup>, Jingsheng Chen<sup>1,5,\*</sup>

<sup>1</sup>Department of Materials Science and Engineering, National University of Singapore, Singapore, 117575, Singapore

<sup>2</sup>Department of Electrical and Computer Engineering, National University of Singapore, Singapore, 117575, Singapore

<sup>3</sup>Centre for Micro- and Nano-Electronics (CMNE), School of Electrical and Electronic Engineering, Nanyang Technological University, 639798, Singapore,

<sup>4</sup>Beijing Superstring Academy of Memory Technology, Beijing, 100176, China

<sup>5</sup>Chongqing Research Institute, National University of Singapore, Chongqing, 401120, China

<sup>6</sup>These authors contributed equally to this work.

\*Authors to whom correspondence should be addressed: [huihui.li@bjsamt.org.cn](mailto:huihui.li@bjsamt.org.cn); [ebktay@ntu.edu.sg](mailto:ebktay@ntu.edu.sg); [msecj@nus.edu.sg](mailto:msecj@nus.edu.sg);

## Abstract

Electrical control of the non-trivial topology in Weyl antiferromagnet is of great interests to develop next-generation spintronic devices. Recent works suggest that spin Hall effect can switch the topological antiferromagnetic order. However, the switching efficiency remains relatively low. Here, we demonstrate effective manipulation of antiferromagnetic order in Weyl semimetal  $Mn_3Sn$  by orbital Hall effect originated from metal Mn or oxide  $CuO_x$ . While  $Mn_3Sn$  is proven to be able to convert orbit current to spin current by itself, we find that inserting a heavy metal layer like Pt with proper thickness can effectively reduce the critical switching current density by one order of magnitude. In addition, we show that the memristor-like switching behavior of  $Mn_3Sn$  can mimic the potentiation and depression processes of a synapse with high linearity, which is beneficial for constructing artificial neural network with high accuracy. Our work paves an alternative way to manipulate topological antiferromagnetic order and may inspire more high-performance antiferromagnetic functional devices.

## Introduction

Topological materials have attracted intensive attentions due to their robust topologically protected states, many exotic properties and promising applications for quantum computing and spintronics [1-2]. According to the dimensionality of electronic bands touching, the topological states of materials can be classified into topological insulators [3-4], Dirac semimetals [5-6] and Weyl semimetals [7-8], etc. Weyl semimetal has the feature of Weyl fermion with the presence of the chiral node (i.e. Weyl node) and the Fermi arc surface states connecting the Weyl-node pair with opposite chirality[9]. The Weyl node is a linearly crossing point of two non-degenerate bands which requires breaking inversion symmetry or time reversal symmetry. In order for developing electronic device, it is essential for effective electrical manipulation of the nontrivial topologic states e.g. Weyl nodes. Magnetic Weyl semimetal is considered as an ideal material candidate since the time reversal symmetry is breaking and the location and enegy of Weyl nodes in the Brillouin zone depend on the magnetization direction [2].  $Mn_3Sn$  is a typical Weyl semimetal and non-collinear antiferromagnet (AFM) [10-13]. As shown in Fig. 1a, the spin structure of  $Mn_3Sn$  consists of two Kagome planes with opposite chirality. This hexagonal spin texture can be considered as a ferroic ordering of a cluster magnetic octupole  $M$  and it breaks time reversal symmetry macroscopically. AFMs have negligible stray field and ultra-fast magnetic dynamics, which helps to overcome the integrability and speed bottlenecks of traditional spintronic devices [14-17]. Furthermore, all-AFM-based magnetic tunnel junctions (MTJ) with a sizable tunneling magnetoresistance (TMR) ratio have recently been demonstrated [18-19].

To date, researchers have demonstrated that spin-orbit torque can manipulate the Weyl nodes in  $Mn_3Sn$  or  $Co_2MnGa$  manifested with the change in anormolous Hall effect (AHE) [20-24], using a similar protocol as for heavy metal/ferromagnets (HM/FM) [25-29] where the spin current generated in heavy metal by spin Hall effect (SHE) is injected into FM and a torque is exerted on FM. As shown in Fig. 1b, the generated spin current induced by current along  $\langle 0001 \rangle$  direction can be directly exerted on the Kagome planes of  $Mn_3Sn$  and induce the magnetization switching. The switching efficiency largely depends on the charge-current-to-spin-current conversion efficiency, i.e., the spin Hall angle (SHA), in the adjacent spin current source layer. To improve the efficiency and reduce the switching current density  $J_c$ , except for exploring novel materials with high SHA, it is also desirable to search alternative mechanisms to realize current-induced switching of topological states with high energy efficiency.

In this work, we propose to utilize orbital Hall effect (OHE) to manipulate the magnetic order in topological AFM. The basic schematic is shown in Fig. 1c. An applied current along  $\langle 0001 \rangle$  direction can induce orbital current in OHE source layer [30-32]. Before the generated orbital current can be exerted on the magnetization of  $Mn_3Sn$ , it need to be converted to spin current by an additional spin-orbit coupling (SOC) [33]. Compared with the limited SHA in spin current source material, it has been demonstrated that orbit current source materials possess a much higher orbit current generation efficiency [34-35]. Therefore, the critical switching current density  $J_c$  is expected to be effectively reduced. Herein, we successfully demonstrate OHE-driven magnetization switching in  $Mn_3Sn$  and prove that the orbit-current-to-spin-current (L-S) conversion can be done either by  $Mn_3Sn$  itself or by inserting a heavy metal with strong

SOC. we have achieved  $J_c$  as low as  $\sim 1 \times 10^{10}$  A/m<sup>2</sup>, which is more than one order of magnitude lower than the common  $J_c$  in SHE-driven framework. Furthermore, we show that the stable memristor-like switching characteristics offers Mn<sub>3</sub>Sn with excellent plasticity to mimic an artificial synapse with linear potentiation and depression processes, which is beneficial for constructing neural networks with high accuracy.

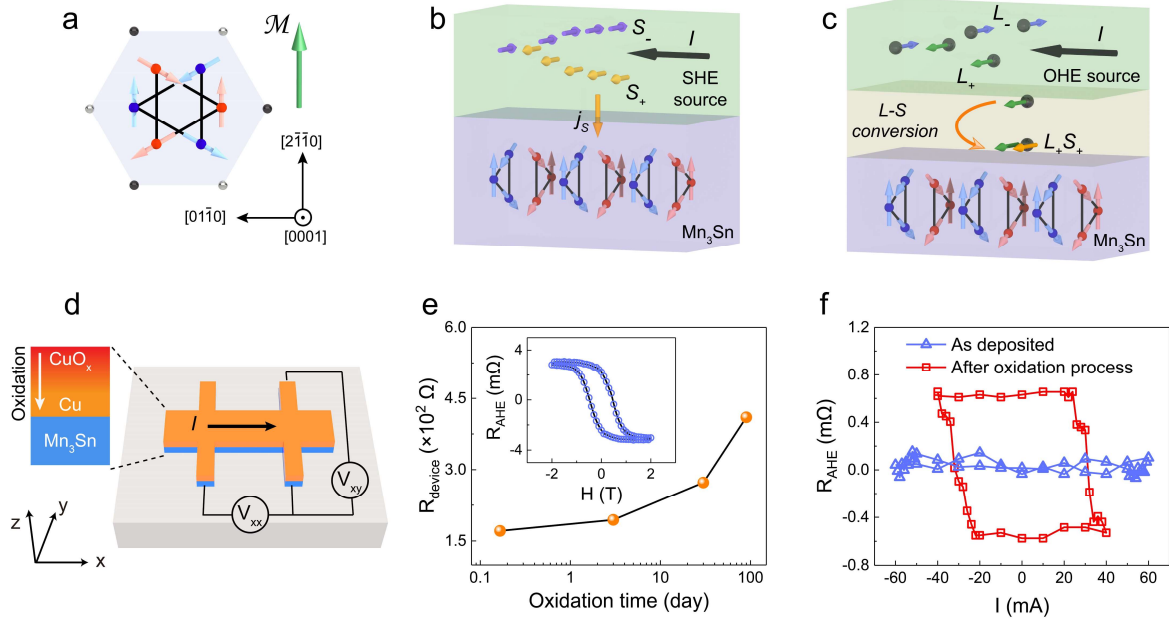


**Fig. 1 Schematic of OHE-driven magnetization switching in Mn<sub>3</sub>Sn.** **a**, Spin structure of Mn<sub>3</sub>Sn. The large blue and red circles (small black and silver circles) represent Mn (Sn) atoms. In two Kagome planes with different chirality, blue and red arrows indicate the magnetic moments of Mn atoms in different layers. The green arrow indicates the  $M$  direction of the formed cluster magnetic octupole. **b**, Schematic of SHE-driven magnetization switching in Mn<sub>3</sub>Sn. Current in spin source layer can generate spin angular momentum  $S_{+(-)}$  which is injected into Mn<sub>3</sub>Sn layer and exerted a torque on the Kagome planes of Mn<sub>3</sub>Sn. **c**, Schematic of OHE-driven magnetization switching. Before being exerted on Mn<sub>3</sub>Sn, orbital angular momentum  $L_{+(-)}$  induced by current in OHE source layer need to be converted to  $S_{+(-)}$ . **d**, Stack structure of Mn<sub>3</sub>Sn/Cu/CuO<sub>x</sub> film and electrical measurement setup. **e**, Longitudinal resistance of Mn<sub>3</sub>Sn/Cu device as a function of oxidation time. Inset illustrates  $R_{\text{AHE}}$  versus applied magnetic field. **f**, Current-induced magnetization switching loops in as-deposited Mn<sub>3</sub>Sn/Cu device and in Mn<sub>3</sub>Sn/Cu/CuO<sub>x</sub> device.

## Results

### OHE-driven magnetization switching in topological Mn<sub>3</sub>Sn

We deposited 40-nm-thick Mn<sub>3</sub>Sn film on thermally oxidized silicon substrates by magnetron sputtering (see details in Methods). By energy dispersive spectrometry (EDS) mapping, the atomic percentage of MnSn alloy is determined to be around Mn<sub>(3.05-3.1)</sub>Sn. The x-ray diffraction (XRD)  $\theta$ - $2\theta$  scans results of the deposited Mn<sub>3</sub>Sn is shown Supplementary Note S1. Compared with pure Si substrate, a clear Mn<sub>3</sub>Sn (0002) crystal peak is observed in the film sample. SQUID

measurement indicates that our film exhibits a tiny out-of-plane magnetization (see Supplementary Note S1). This tiny out-of-plane hysteresis loop suggests there exist crystalline grains with its Kagome plane in the film normal since the spin canting is in the (0001) Kagome plane. We further carried out magneto-transport and anomalous Nernst effect (ANE) measurements to confirm the Weyl semimetal of our deposited Mn<sub>3</sub>Sn films. Planar Hall effect (PHE) and in-plane angular magnetoresistance (AMR) are shown in Fig. S1c. The PHE and AMR follow the functions  $R_{xy} = -\Delta R \sin \theta \cos \theta$  and  $R_{xx} = R_{\perp} - \Delta R \cos^2 \theta$ , respectively, where  $\Delta R = R_{\perp} - R_{\parallel}$ , and  $R_{\perp}$  and  $R_{\parallel}$  are the resistances when the magnetic field directions are perpendicular and parallel to the charge current direction, respectively. These are consistent with the feature of the chiral anomaly induced PHE and AMR in Weyl semimetal [9,20]. Comparing to the effect of magnetization, ANE in Weyl semimetal is much enhanced due to the Weyl nodes around Fermi level [11]. The large ANE and small magnetization further confirm that our Mn<sub>3</sub>Sn films are the Weyl semimetal (Supplementary Fig. S1b and c).

It has been widely demonstrated that OHE can be observed in the naturally oxidized Cu [39-40]. Thus, we firstly choose oxidized Cu to verify the OHE effect on the magnetization switching of Mn<sub>3</sub>Sn antiferromagnet. As shown in inset of Fig. 1d, we firstly deposited a Cu layer on the Mn<sub>3</sub>Sn layer and then follow the method in Ref [40] to naturally oxidize Cu at atmosphere for different time. The films were fabricated into Hall bar device of 5  $\mu\text{m}$  width to implement magneto-transport measurement. The schematic setup of the measurement is illustrated in Fig. 1d. The longitudinal resistance shows a continuous increase with oxidation time, which suggests the gradual oxidation of Cu layer with the time. We then measure the AHE resistance  $R_{\text{AHE}}$  (inset in Fig. 1e) as a function of the out-of-plane magnetic field to estimate the switchable magnetic domains which corresponds to the crystalline grains with Kagome plane in the film normal. In the absence of magnetic field, there exist two stable magnetic states which correspond to the magnetic octupole  $M$  along  $\pm z$  directions, respectively.

We then carry out current-induced switching experiments (Fig. 1f). Since Cu is a light metal with negligible SOC, current-induced magnetization switching is absent in the as-deposited Mn<sub>3</sub>Sn/Cu film. As a comparison, a deterministic magnetization switching loop, corresponding to a switching ratio of  $\sim 25\%$ , is well achieved in the device after natural oxidatization process of the Cu. We are also aware that several works reported current-induced switching in Mn<sub>3</sub>Sn single layer with specific crystal configuration[41-42]. However, we didn't observe any switching phenomenon in our deposited Mn<sub>3</sub>Sn single layer (Supplementary Note S2), verifying that the magnetization switching driving force indeed comes from the achieved CuO<sub>x</sub> layer. Additionally, it is reported that only when the FM like NiFe exhibits a relatively high SOC, one can observe a sizable effective SHA in FM/Cu/CuO<sub>x</sub> heterostructure [33,40]. It is because the orbital current originated from CuO<sub>x</sub> must complete the  $L$ - $S$  conversion process shown in Fig. 1c to manipulate the magnetic dynamics in FM. Our deterministic switching results in Mn<sub>3</sub>Sn/Cu/CuO<sub>x</sub> device directly prove that Mn<sub>3</sub>Sn itself can complete the  $L$ - $S$  conversion process like what NiFe does and the spin current converted from orbit current is then to switch the magnetization of Mn<sub>3</sub>Sn layer. More experimental evidences related to SOC and  $L$ - $S$  conversion in Mn<sub>3</sub>Sn will be presented in the next section.

Note that, for practical use, it is important to quantitatively control the orbital Hall angle in the device. In such case, metallic OHE sources have an application edge over naturally oxidized Cu. We thus employ an heterostructure composed of Mn<sub>3</sub>Sn (40 nm)/Pt( $t_{\text{Pt}}$ )/Mn( $t_{\text{Mn}}$ ) trilayer (Fig. 2a) to further investigate the detailed OHE manipulation characteristics of topological magnetization. Mn is theoretically predicted to possess a large orbital Hall angle ( $\sim 18$ ) [35]. The inserted Pt layer serve as an additional  $L$ - $S$  conversion layer which helps to gain more spin torques [33,43]. In a device where  $t_{\text{Pt}} = 2$  nm and  $t_{\text{Mn}} = 10$  nm, deterministic OHE-driven magnetization switching in Mn<sub>3</sub>Sn is achieved as well (see detailed switching loops in Supplementary Note S3). An external magnetic field  $H_{\text{ex}}$  is required to break the in-plane symmetry during the switching process. When reversing the direction of  $H_{\text{ex}}$ , the switching polarity also changes. This switching characteristic is very similar to the SHE-induced switching protocol for FMs. Moreover, we have observed a  $H_{\text{ex}}$ -dependent switching ratio tendency in the sample. The switching ratio is defined as  $\Delta R_{\text{c}}/\Delta R_{\text{H}}$ , where  $\Delta R_{\text{c}}$  and  $\Delta R_{\text{H}}$  are current-induced and field-induced change of  $R_{\text{AHE}}$ . As shown in Fig. 2b, as the absolute value of  $H_{\text{ex}}$  increases, the switching ratio will first increase and then saturate when exceeds 2 kOe. The saturated switching ratio is around 27%, which is comparable with other reported value [20,36,44]. This relatively small switching ratio can be explained by the fact that in-plane torques only allow the Kagome planes to rotate between two energy minimum states with  $\theta = \pm\pi/6$  (see Fig. 2c) according to the symmetry analysis [20]. Note that all the following switching experiments in this work were carries out under  $H_{\text{ex}} = 2$  kOe, unless specified.

An important difference between switching in FM and switching in Mn<sub>3</sub>Sn is the impact of applied current pulse width. In FM system, a thermally activated switching model, in which  $J_{\text{c}}$  decreases exponentially with the increasing pulse width, is widely accepted [45]. In Fig. 2d, we plot  $R_{\text{AHE}}$  as a function of the applied charge current density  $J$  in Pt/Mn bilayer with different pulse width. Clearly,  $J_{\text{c}}$  in Mn<sub>3</sub>Sn is almost insensitive to the current pulse width which varies from 10  $\mu\text{s}$  to 500  $\mu\text{s}$  (see Fig. 2d). This insensitivity indicates that our deposited Mn<sub>3</sub>Sn possesses a good thermal stability, which is beneficial for the device scalability. We also notice that the achieved  $R_{\text{AHE}}-J$  switching loops are quite ‘tilted’, i.e., there exists a series of intermediate states. As shown in Fig. 2e, a series of minor switching loops can be achieved by limiting the maximum value at negative current range. In Supplementary Note S4, we show that controlling the applied out-of-plane magnetic field can also achieve similar minor loops. The stable existence of these minor loops reveals that the intermediate states are non-volatile and can be recovered to the same initial state by applying a current density  $J \sim 9 \times 10^{10}$  A/m<sup>2</sup>. This switching characteristic indicates that the Mn<sub>3</sub>Sn device can possibly memorize the past electrical current pulse and be adapted as a memristor. We will further investigate the potential application of this memristor-like behavior in neuromorphic computing in the last section.

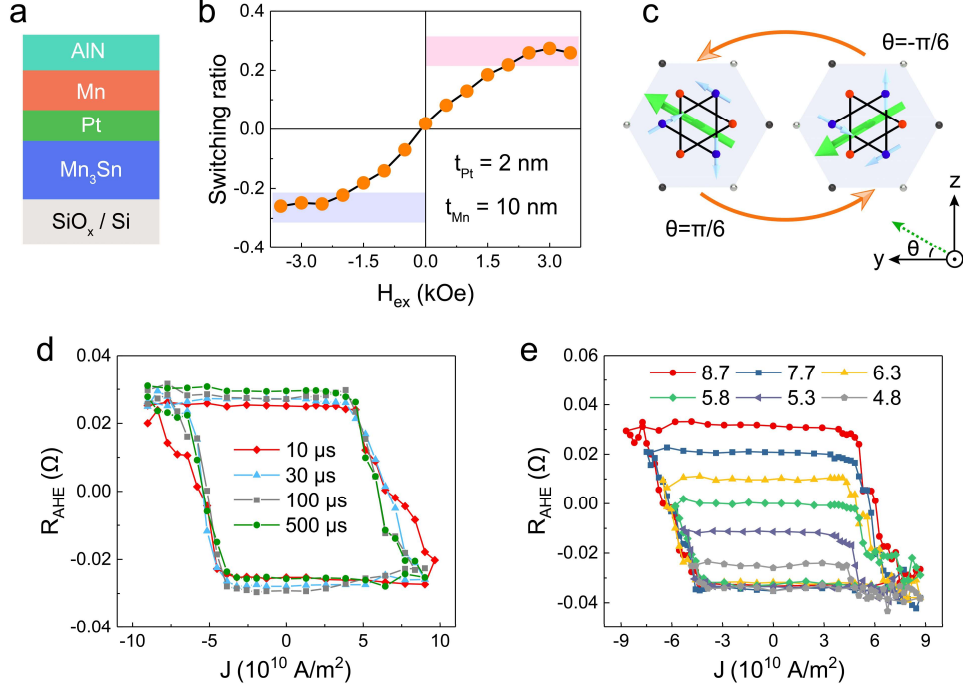


**Fig. 2 OHE-driven magnetization switching in  $\text{Mn}_3\text{Sn}/\text{Pt}(2 \text{ nm})/\text{Mn}(10 \text{ nm})$ .** **a**, Schematic of the  $\text{Mn}_3\text{Sn}/\text{Pt}/\text{Mn}$  heterostructure. **b**, Schematic of two stable magnetic states in  $\text{Mn}_3\text{Sn}$  during OHE-driven switching dynamics. **c**, OHE-driven switching ratio as a function of  $H_{\text{ex}}$ . The ratio saturates when  $H_{\text{ex}}$  exceeds 2 kOe. **d**,  $R_{\text{AHE}}-J$  switching loops with different applied pulse width. **e**, Minor switching loops of the sample by limiting the maximum current value in negative range.

### OHE source layer dependence of switching efficiency

To further verify that the observed switching behaviors are dominant by OHE in  $\text{Mn}_3\text{Sn}/\text{Pt}/\text{Mn}$  and to optimize the switching performance, we implemented current-induced switching experiments in samples with different Pt and Mn thicknesses. We first investigate the impact of  $t_{\text{Pt}}$  by fixing  $t_{\text{Mn}}$  to 10 nm and varying  $t_{\text{Pt}}$  from 0.5 nm to 6 nm. In all the samples, deterministic switching is observed, while the switching polarity remains the same (see Supplementary Note S3). Fig. 3a plots  $J_c$  as a function of Pt thickness  $t_{\text{Pt}}$ . This tendency can be separated into 3 stages: 1) when  $t_{\text{Pt}} \geq 4 \text{ nm}$ ,  $J_c$  keeps at a stable plateau; 2) when  $1 \text{ nm} \leq t_{\text{Pt}} < 4 \text{ nm}$ ,  $J_c$  decreases with  $t_{\text{Pt}}$  decreasing; 3) when  $t_{\text{Pt}} < 1 \text{ nm}$ ,  $J_c$  starts to slightly increase with decreasing  $t_{\text{Pt}}$ . It is known that the effective SHA of Pt will first increase and then saturate when  $t_{\text{Pt}}$  increases from 0 nm to 4-5 nm [46]. The change of  $J_c$  with  $t_{\text{Pt}}$  can be understood as follows. At stage 1, SHE from Pt dominates the switching and OHE barely participates in the process. At stage 2 and 3, OHE gradually dominates the switching process, since the observed  $J_c-t_{\text{Pt}}$  tendency in this region is opposite to the  $J_c-t_{\text{Pt}}$  tendency in conventional SHE-dominant system (see detailed switching results of  $\text{Mn}_3\text{Sn}/\text{Pt}$  in Supplementary Note S2).

The minimum  $J_c$  appears at around  $t_{\text{Pt}} = 1 \text{ nm}$ , revealing that the  $L$ - $S$  conversion efficiency in  $\text{Mn}_3\text{Sn}/\text{Pt}/\text{Mn}$  system maximizes at this point. To better quantify the switching efficiency, we measured the effective SHA in  $\text{Co}/\text{Pt}(t_{\text{Pt}})/\text{Mn}(10 \text{ nm})$  heterostructure by spin-torque

ferromagnetic resonance (ST-FMR) technique (see details in Supplementary Note S5). As shown in Fig. 3b, when  $t_{\text{Pt}}$  increases from 1 nm to 6 nm, the effective SHA will first increase and then decrease. The highest SHA ( $\sim 0.4$ ) appears when  $t_{\text{Pt}}$  is around 2-3 nm, which is comparable with other reported values [33-34,43]. We also notice that this optimal SHA point is shifted from the optimal  $J_c$  point in  $\text{Mn}_3\text{Sn}/\text{Pt}/\text{Mn}$  system. This shifted optimal point can be explained by the fact that  $\text{Mn}_3\text{Sn}$  possesses higher SOC than the 3d transition metal Co [13]. It is also consistent with our previous switching results in  $\text{Mn}_3\text{Sn}/\text{Cu}/\text{CuO}_x$  device where the Pt layer is absent, confirming again that extra  $L$ - $S$  conversion indeed happens in  $\text{Mn}_3\text{Sn}$ .

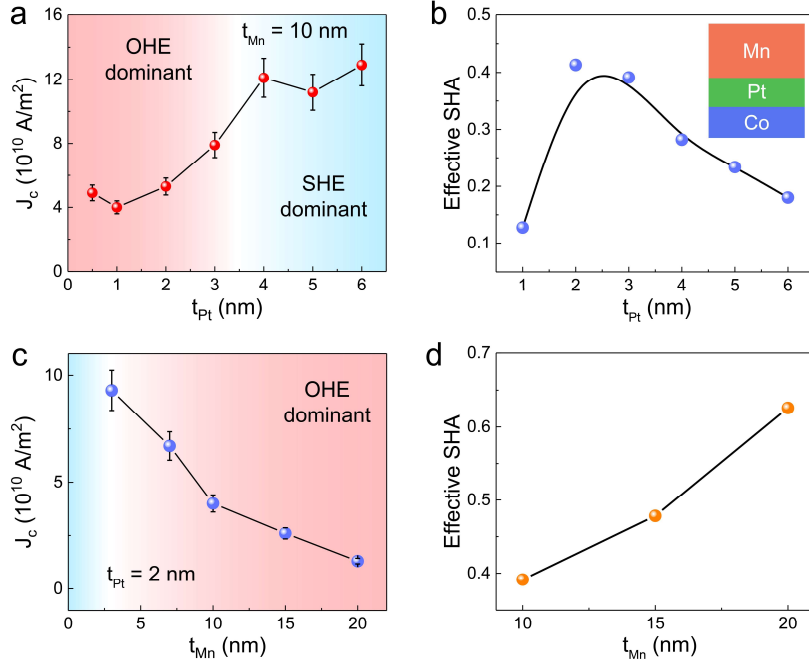


**Fig. 3 OHE source layer dependence of the switching efficiency.** **a**,  $J_c$  as a function of Pt thickness  $t_{\text{Pt}}$  with a fixed Mn thickness ( $t_{\text{Mn}} = 10$  nm). When  $t_{\text{Pt}} \leq 3$  nm, the switching dynamics is dominated by OHE (red region). When  $t_{\text{Pt}} > 3$  nm, SHE (blue region) dominates the switching dynamics. **b**, Effective SHA in Co/Pt/Mn as a function of  $t_{\text{Pt}}$  while  $t_{\text{Mn}}$  remains at 10 nm. Inset shows the film stack. **c**,  $J_c$  as a function of  $t_{\text{Mn}}$  with a fixed  $t_{\text{Pt}}$  (2 nm). A monotonic decreasing tendency can be achieved. **d**, Effective SHA as a function of  $t_{\text{Mn}}$  while  $t_{\text{Pt}}$  remains at 3 nm.

We then investigate the impact of  $t_{\text{Mn}}$  by fixing  $t_{\text{Pt}}$  to 2 nm and varying  $t_{\text{Mn}}$  from 3 to 20 nm. As shown in Fig. 3c, a monotonic decreasing  $J_c$ - $t_{\text{Mn}}$  tendency can be achieved. When  $t_{\text{Mn}} = 20$  nm,  $J_c$  is reduced to  $\sim 1 \times 10^{10}$  A/m $^2$ , which is more than one order of magnitude lower than  $J_c$  in  $\text{Mn}_3\text{Sn}/\text{Pt}$  bilayer [20]. This tendency is consistent with the  $t_{\text{Mn}}$ -dependent SHA tendency in Co/Pt/Mn system (see Fig. 3d). When  $t_{\text{Mn}}$  increases from 10 nm to 20 nm, the effective SHA monotonically increases. At  $t_{\text{Mn}} = 20$  nm, the effective SHA is determined to be around 0.64. We consider this unsaturated effective SHA within a large  $t_{\text{Mn}}$  range as another important characteristic of OHE. According to the drift-diffusion equation, the orbital Hall angle of Mn  $\theta_{\text{Mn}}$ , which is defined as the charge-current-to-orbital-current conversion efficiency, can be described by  $\theta_{\text{Mn}} = \sigma_{\text{Mn}}[1 - \text{sech}(t_{\text{Mn}}/\lambda_{\text{Mn}})]$ , where  $\sigma_{\text{Mn}}$  and  $\lambda_{\text{Mn}}$  are the orbital Hall conductivity and orbital diffusion length of Mn, respectively.  $\lambda_{\text{Mn}}$  ( $\sim 11$  nm) is theoretically expected to be much longer than the typical spin diffusion length of conventional heavy metal (1-2 nm for Pt) [34]. As a result,  $\theta_{\text{Mn}}$  should have a much longer saturation length ( $> 20$  nm in our work) than



the SHA saturation length in Pt (typically 5 nm). Given a fixed L-S conversion efficiency, a larger  $\theta_{\text{Mn}}$  will certainly lead to a larger effective SHA in the system as well as a lower  $J_c$ .

### Neuromorphic computing based on OHE manipulation of Mn<sub>3</sub>Sn

Artificial synapses are considered as an ideal hardware to implement neuromorphic computing [47-50]. Recent works suggest the current-induced magnetization switching process in ferro- and ferri-magnetic materials can mimic the long-term depression (LTD) and the long-term potentiation (LTP) functions of synapses, following a general domain nucleation theory [51-52]. However, the linearity of achieved LTD (LTP) processes, which is considered as a fundamental parameter for constructing high-accuracy artificial neural network (ANN), has arrived at a ceiling, because of the limited magnetic domain size. In such case, Mn<sub>3</sub>Sn is expected to be a better material platform, since the AFM nature of Mn<sub>3</sub>Sn can reduce the magnetic dipole effect and thus allow the existence of more tiny magnetic domains in the crossbar area than ferromagnet does. Moreover, the random magnetic domain switching phenomena brought by thermal fluctuation is also expected to be suppressed, given the low OHE-driven critical switching current density as well as the good thermal stability of Mn<sub>3</sub>Sn.

In Fig. 2e, we have already shown that the OHE-driven switching process of Mn<sub>3</sub>Sn exhibits a memristor-like behavior. Here, given the normalized  $R_{\text{AHE}}$  detected during the switching can be defined as the weight ( $G$ ) of the artificial synapse, we demonstrate the realization of LTD and LTP functions in a Mn<sub>3</sub>Sn/Pt(2 nm)/Mn(10 nm) device. As shown in Fig. 4a, to achieve such processes, 120 negative (positive) current pulses of fixed amplitude are applied. The current pulse amplitude is  $\sim 4.5 \times 10^{10}$  A/m<sup>2</sup>, which corresponds to the very beginning switching point of the device. Interestingly, we found the achieved LTD (LTP) processes show very high linearity. To better quantify the linearity performance, the nonlinearity ( $NL$ ) of weight update is defined as  $NL = \frac{\max|G_P(n) - G_D(121-n)|}{(G_{\max} - G_{\min})}$  for  $n = 1$  to 120,

where  $G_P(n)$  and  $G_D(n)$  are the normalized  $R_{\text{AHE}}$  values after the  $n^{\text{th}}$  potentiation pulse and  $n^{\text{th}}$  depression pulse.  $G_{\max}$  and  $G_{\min}$  represent the maximum  $G_P(n)$  after 120 potentiation pulses and minimum  $G_D(n)$  at initial state. Here, a very small  $NL$  value ( $\sim 0.166$ ) is determined, indicating that our Mn<sub>3</sub>Sn-based artificial synapse possesses a similar LTD (LTP) process to an ideal device (see Supplementary Note S6).

To better evaluate the performance of the proposed synapse, an ANN with a  $100 \times 100$  Mn<sub>3</sub>Sn-based memory array was then constructed to implement pattern recognition task (see Fig.4b). The subsequent learning processes followed the synaptic weight change processes shown in Fig. 4a. Each memory cell serves as a synapse to connect pre- and post-neurons, and the synaptic weight of each cell was represented by the gray level of each pixel. The  $100 \times 100$  pixels of initial input image taken from the Yale Face Database B is employed for the pattern recognition task [53], and the gray variation of each pixel is real-time stored in each cell with the increasing learning epochs. Fig. 4c compares the image evolution with various numbers of learning epochs during the learning process for the experimental and ideal devices. For the quantitative analysis of learning efficiency, the learning accuracy at every 5 epochs, which is defined as the difference between the original image and learned image, can be obtained (see



details in Supplementary Note S6). As shown in Fig. 4d, the learning accuracy rate of the experimental device is 97.5%, which is only slightly lower than that of the ideal device (~99.5%). The above simulation results strongly suggest the high application potential of our Mn<sub>3</sub>Sn-based spintronic device in neuromorphic computing.

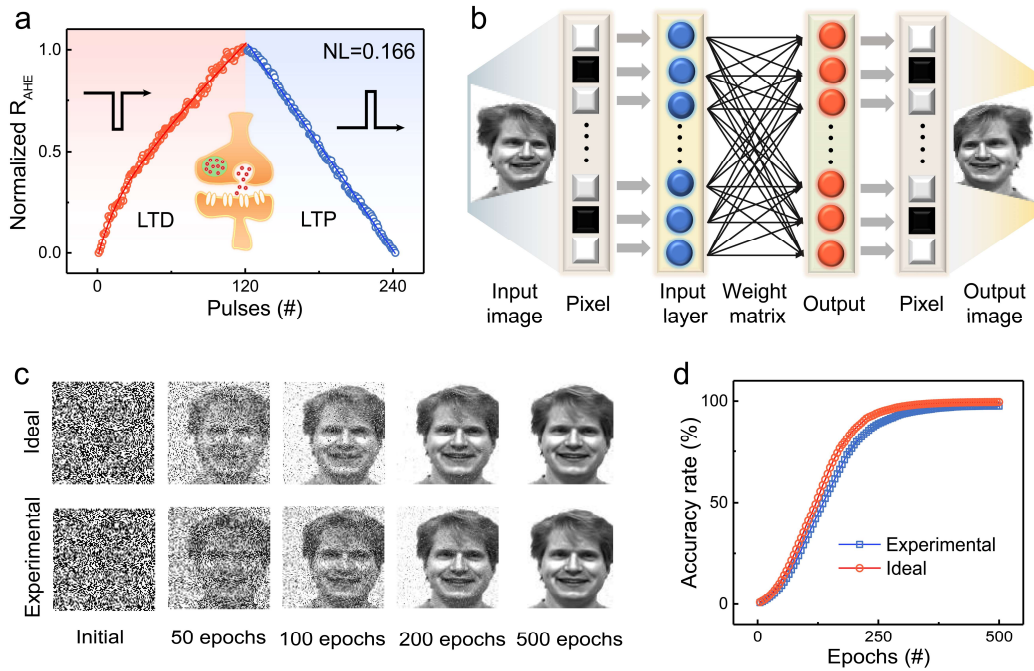


**Fig. 4 ANN system with Mn<sub>3</sub>Sn-based artificial synapse.** (a) LTD and LTP process with high linearity in Mn<sub>3</sub>Sn/Pt(2 nm)/Mn(10 nm) device. (b) Schematic of the constructed ANN with 100 × 100 memory cells for image recognition task. (c) Evolution of the images in the learning processes with the experimental and ideal devices. The image is taken from Yale Face Database B [53]. (d) Image accuracy rates as a function of learning epochs in constructed ANN.

## Conclusions

In summary, we have demonstrated that OHE can serve as an effective electrical method to manipulate the topological magnetization of antiferromagnets. We prove that Mn<sub>3</sub>Sn can directly convert the orbital current from the OHE sources, e.g., metals (Mn) and oxides (CuO<sub>x</sub>), to spin current. We also show that an inserted Pt layer between Mn<sub>3</sub>Sn and OHE source can enhance the L-S conversion efficiency. By adjusting the thickness of Pt and Mn, the critical switching current density can be reduced to as low as  $\sim 1 \times 10^{10}$  A/m<sup>2</sup>. In addition, we show that the OHE-driven switching process in Mn<sub>3</sub>Sn can mimic the LTD and LTP process with high linearity in an artificial synapse, which can be further utilized to construct ANN system with high image recognition accuracy. Finally, given TMR has been reported in AFM-MTJ, it is possible to incorporate the presented OHE-driven Mn<sub>3</sub>Sn switching scheme in an OHE-based AFM MTJ devices. Our finding goes beyond the conventional paradigm of using spin current to manipulate AFM's order, and offers an alternative to integrate topological AFM in future diverse spintronic devices.

## Methods

**Sample growth and device fabrication:**  $\text{Mn}_3\text{Sn}(40)/\text{Pt}(0-6)/\text{Mn}(0-20)/\text{AlN}(5)$  and  $\text{Mn}_3\text{Sn}(40)/\text{Cu}(10)$  stacks (thickness in nm) are deposited on thermally oxidized silicon substrates by DC and RF magnetic sputtering (AJA) under a base pressure lower than  $3 \times 10^{-8}$  Torr. AlN is an insulating capping layer.  $\text{Mn}_3\text{Sn}$  are deposited by co-sputtering of  $\text{Mn}_{2.5}\text{Sn}$  and Mn targets at room temperature, followed by annealing in situ at 500 °C for 1 hour. After cooling down to room temperature, the following Pt/Mn/AlN or Cu layers are deposited. For the oxidation process,  $\text{Mn}_3\text{Sn}/\text{Cu}$  films were exposed to dry atmosphere for a set time. Then, AlN is deposited to stop Cu from being further oxidized. The films were fabricated into Hall bar devices of 5  $\mu\text{m}$  width by standard lithography and ion milling techniques.

**Electrical measurement:** For transverse and longitudinal resistance measurements, an ac current of 317.3 Hz was applied along the x axis, while SR830 and Zurich lock-in amplifiers are used to detect the voltage. For current-induced switching and neuromorphic functions, electrical current pulses (width from 10 to 500  $\mu\text{s}$ ) were applied. After each pulse, we wait for 5 s to avoid the Joule heating and use a small ac current to read out the AHE voltage. For ST-FMR measurement, a Rohde & Schwarz SMB 100A signal generator was used to provide the modulated microwave. The rectifying voltage was collected using a lock-in amplifier.

## Author contributions

J.S.C., B.K.T, and H.H.L. supervised the project; Z.Y.Z. and J.S.C conceived the idea; Z.Y.Z. deposited the films and fabricated the devices with help from T.Y.Z., H.H.L., L.X.J., Y.D.G. and R.X.; L.Z.R. performed the SQUID experiment; S.S. implemented the XRD measurement; Z.Y.Z. and T.Y.Z. implemented the electrical transport measurement and analyzed the data with help from H.A.Z., Q.H.Z. and J.Q.L.; T.Z. performed the neuromorphic function simulation; T.T.Z., G.L.W. and C.Z. contributed to the data interpretation. Z.Y.Z., T.Y.Z., T.Z. and J.S.C. co-wrote the manuscript. All the authors read and commented on the manuscript.

## Acknowledgements

The research is supported by the Singapore Ministry of Education MOE-T2EP50121-0011, MOE-T2EP50121-0001, MOE Tier 1: 22-4888-A0001, A\*STAR RIE2020 Advanced Manufacturing and Engineering (AME) Programmatic Grant- A20G9b0135. The authors acknowledge the use of the Yale Face Database.

## Competing financial interests

The authors declare no competing financial interest.

## Data availability

The data that support the findings of this study are available from the corresponding authors upon reasonable request.

## References

1. Nayak, C. et al. Non-Abelian anyons and topological quantum computation. *Rev. Mod. Phys.* **80**, 1083 (2008).
2. Bernevig, B. A., Claudia, F. & Haim, B. Progress and prospects in magnetic topological materials. *Nature* **603**, 41-51 (2022).
3. Fu, L., Charles, L. K. & Eugene J. M. Topological insulators in three dimensions. *Phys. Rev. Lett.* **98**, 106803 (2007).
4. Chen, Y. L. et al. Experimental realization of a three-dimensional topological insulator,  $\text{Bi}_2\text{Te}_3$ . *Science* **325**, 178-181 (2009).
5. Liu, Z. K. et al. Discovery of a three-dimensional topological Dirac semimetal,  $\text{Na}_3\text{Bi}$ . *Science* **343**, 864-867 (2014).
6. Young, S. M. et al. Dirac semimetal in three dimensions. *Phys. Rev. Lett.* **108**, 140405 (2012).
7. Xu, S. Y. et al. Discovery of a Weyl fermion semimetal and topological Fermi arcs. *Science* **349**, 613-617 (2015).
8. Burkov, A. A. & Balents, L. Weyl semimetal in a topological insulator multilayer. *Phys. Rev. Lett.* **107**, 127205 (2011).
9. Jia, S. et al. Weyl semimetals, Fermi arcs and chiral anomalies. *Nat. Mater.* **15**, 1140-1144 (2016).
10. Nakatsuji, S., Kiyohara, N. & Higo, T. Large anomalous Hall effect in a non-collinear antiferromagnet at room temperature. *Nature* **527**, 212-215 (2015).
11. Ikhlas, M. et al. Large anomalous Nernst effect at room temperature in a chiral antiferromagnet. *Nat. Phys.* **13**, 1085-1090 (2017).
12. Kimata, M. et al. Magnetic and magnetic inverse spin Hall effects in a non-collinear antiferromagnet. *Nature* **565**, 627-630 (2019).
13. Yang, H. et al. Topological Weyl semimetals in the chiral antiferromagnetic materials  $\text{Mn}_3\text{Ge}$  and  $\text{Mn}_3\text{Sn}$ . *New J. Phys.* **19**, 015008 (2017).
14. Jungwirth, T., Marti, X., Wadley, P. & Wunderlich, J. Antiferromagnetic spintronics. *Nat. Nanotechnol.* **11**, 231-241 (2016).
15. Peng, S. et al. Exchange bias switching in an antiferromagnet/ferromagnet bilayer driven by spin-orbit torque. *Nat. Electron.* **3**, 757-764 (2020).
16. Shi, J. et al. Electrical manipulation of the magnetic order in antiferromagnetic PtMn pillars. *Nat. Electron.* **3**, 92-98 (2020).
17. Li, J. et al. Spin current from sub-terahertz-generated antiferromagnetic magnons. *Nature* **578**, 70-74 (2020).
18. Qin, P. et al. Room-temperature magnetoresistance in an all-antiferromagnetic tunnel junction. *Nature* **613**, 485-489 (2023).
19. Chen, X. et al. Octupole-driven magnetoresistance in an antiferromagnetic tunnel junction. *Nature* **613**, 490-495 (2023).
20. Tsai, H. et al. Electrical manipulation of a topological antiferromagnetic state. *Nature* **580**,

- 608-613 (2020).
21. Higo, T. et al. Perpendicular full switching of chiral antiferromagnetic order by current. *Nature* **607**, 474-479 (2022).
  22. Takeuchi, Y. et al. Chiral-spin rotation of non-collinear antiferromagnet by spin-orbit torque. *Nat. Mater.* **20**, 1364-1370 (2021).
  23. Ren, L. et al. Manipulation of the topological ferromagnetic state in a weyl semimetal by spin-orbit torque. *Nano Lett.* **23**, 3394-3400 (2023).
  24. Han, J. et al. Current-induced switching of a ferromagnetic Weyl semimetal Co<sub>2</sub>MnGa. *Appl. Phys. Lett.* **119**, 212409 (2021).
  25. Miron, I. M. et al. Perpendicular switching of a single ferromagnetic layer induced by in-plane current injection. *Nature* **476**, 189-193 (2011).
  26. Liu, L. et al. Spin-torque switching with the giant spin Hall effect of tantalum. *Science* **336**, 555-558 (2012).
  27. Liu, L. et al. Symmetry-dependent field-free switching of perpendicular magnetization. *Nat. Nanotechnol.* **16**, 277-282 (2021).
  28. Wang, M. et al. Field-free switching of a perpendicular magnetic tunnel junction through the interplay of spin-orbit and spin-transfer torques. *Nat. Electron.* **1**, 582-588 (2018).
  29. Zheng, Z. et al. Field-free spin-orbit torque-induced switching of perpendicular magnetization in a ferrimagnetic layer with a vertical composition gradient. *Nat. Commun.* **12**, 4555 (2021).
  30. Go, D. et al. Intrinsic spin and orbital Hall effects from orbital texture. *Phys. Rev. Lett.* **121**, 086602 (2018).
  31. Kontani, H. et al. Giant orbital Hall effect in transition metals: Origin of large spin and anomalous Hall effects. *Phys. Rev. Lett.* **102**, 016601 (2009).
  32. Go, D. et al. Orbitronics: Orbital currents in solids. *Europhys. Lett.* **135**, 37001 (2021).
  33. Ding, S. et al. Harnessing orbital-to-spin conversion of interfacial orbital currents for efficient spin-orbit torques. *Phys. Rev. Lett.* **125**, 177201 (2020).
  34. Sala, G. & Gambardella, P. Giant orbital Hall effect and orbital-to-spin conversion in 3d, 5d, and 4f metallic heterostructures. *Phys. Rev. Res.* **4**, 033037 (2022).
  35. Jo, D., Go, D. & Lee, H. W. Gigantic intrinsic orbital Hall effects in weakly spin-orbit coupled metals. *Phys. Rev. B* **98**, 214405 (2018).
  36. Yan, G. Q. et al. Quantum sensing and imaging of spin-orbit-torque-driven spin dynamics in the non-collinear antiferromagnet Mn<sub>3</sub>Sn. *Adv. Mat.* **34**, 2200327 (2022).
  37. Nandy, S. et al. Chiral anomaly as the origin of the planar Hall Effect in Weyl semimetals. *Phys. Rev. Lett.* **119**, 176804 (2017).
  38. Kumar, N. et al. Planar Hall effect in the Weyl semimetal GdPtBi. *Phys. Rev. B* **98**, 041103 (2018).
  39. Go, D. et al. Orbital Rashba effect in a surface-oxidized Cu film. *Phys. Rev. B* **103**, L121113 (2021).
  40. An, H. et al. Spin-torque generator engineered by natural oxidation of Cu. *Nat. Commun.* **7**, 13069 (2016).
  41. Xie, H. et al. Magnetization switching in polycrystalline Mn<sub>3</sub>Sn thin film induced by self-generated spin-polarized current. *Nat. Commun.* **13**, 5744 (2022).
  42. Deng, Y. et al. All-electrical switching of a topological non-collinear antiferromagnet at

- room temperature. *Nat. Sci. Rev.* **10**, nwac154 (2023).
43. Lee, S. et al. Efficient conversion of orbital Hall current to spin current for spin-orbit torque switching. *Commun. Phys.* **4**, 234 (2021).
  44. Pal, B. et al. Setting of the magnetic structure of chiral kagome antiferromagnets by a seeded spin-orbit torque. *Sci. Adv.* **8**, eabo5930 (2022).
  45. Wang, M. et al. Current-induced magnetization switching in atom-thick tungsten engineered perpendicular magnetic tunnel junctions with large tunnel magnetoresistance. *Nat. Commun.* **9**, 671 (2018).
  46. Wang, Y. et al. Determination of intrinsic spin Hall angle in Pt. *Appl. Phys. Lett.* **105**, 152412 (2014).
  47. Xia, Q. & Yang, J. Memristive crossbar arrays for brain-inspired computing. *Nat. Mater.* **18**, 309-323 (2019).
  48. Wang, Z. et al. Toward a generalized Bienenstock-Cooper-Munro rule for spatiotemporal learning via triplet-STDP in memristive devices. *Nat. Commun.* **11**, 1510 (2020).
  49. Ielmini, D. & Wong H. In-memory computing with resistive switching devices, *Nat. Electron.* **1**, 333-343 (2018).
  50. Guo, R. et al. Ferroic tunnel junctions and their application in neuromorphic networks. *Appl. Phys. Rev.* **7**, 011304 (2020).
  51. Liu, J. et al. Compensated ferrimagnet based artificial synapse and neuron for ultrafast neuromorphic computing. *Adv. Funct. Mater.* **32**, 2107870 (2022).
  52. Zhou, J. et al. Spin-orbit torque-induced domain nucleation for neuromorphic computing. *Adv. Mater.* **33**, 2103672 (2021).
  53. Belhumeur, P., Hespanha, J. & Kriegman, D. Eigenfaces vs. fisherfaces: Recognition using class specific linear projection. *IEEE Trans. Pattern Anal. Mach. Intell.* **19**, 711 (1997).